ACS OMEGA

http://pubs.acs.org/journal/acsodf

Article

# Two-Dimensional $NH_4V_3O_8$ Nanoflakes as Efficient Energy Conversion and Storage Materials for the Hydrogen Evolution Reaction and Supercapacitors

Phuoc-Anh Le,* Van-Qui Le, Thien Lan Tran, Nghia Trong Nguyen, Thi Viet Bac Phung,* and Van An Dinh

Cite This: *ACS Omega* 2022, 7, 25433−25442

Read Online

ACCESS | Metrics & More | Article Recommendations | Supporting Information

**ABSTRACT:** Herein, for the first time, we present two-dimensional (2D) $NH_4V_3O_8$ nanoflakes as an excellent material for both energy conversion of the hydrogen evolution reaction and storage of supercapacitors by a simple and fast two-step synthesis, which exhibit a completely sheet-like morphology, high crystallinity, good specific surface area, and also stability, as determined by thermogravimetric analysis. The 2D-$NH_4V_3O_8$ flakes show an acceptable hydrogen evolution performance in 0.5 M $H_2SO_4$ on a glassy carbon electrode (GCE) coated with 2D-$NH_4V_3O_8$, which results in a low overpotential of 314 mV at −10 mA $cm^{-2}$ with an excellent Tafel slope as low as 90 mV $dec^{-1}$. So far, with the main focus on energy storage, 2D-$NH_4V_3O_8$ nanoflakes were found to be ideal for supercapacitor electrodes. The $NH_4V_3O_8$ working electrode in 1 M $Na_2SO_4$ shows an excellent electrochemical capability of 274 F $g^{-1}$ at 0.5 A $g^{-1}$ for a maximum energy density of 38 W h $kg^{-1}$ at a power density as high as 250 W $kg^{-1}$. Moreover, the crystal structure of 2D-$NH_4V_3O_8$ is demonstrated by density functional theory (DFT) computational simulation using three functionals, GGA, GGA + *U*, and HSE06. The simple preparation, low cost, and abundance of the $NH_4V_3O_8$ material provide a promising candidate for not only energy conversion but also energy-storage applications.

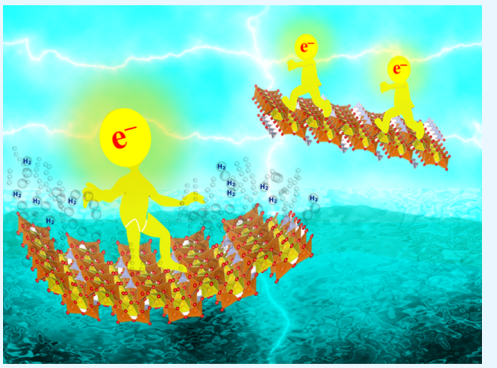


## 1. INTRODUCTION

With the rapidly growing renewable energy sector, the major problems of limited fossil fuel and global warming have led to an urgent need for electrochemical energy storage and conversion.[1,2] Currently, more and more energy-storage devices for supercapacitors and energy-conversion systems for the hydrogen evolution reaction have been reported.

Among various types of energy-storage devices, supercapacitors are prime candidates because of their greater safety, higher energy density, longer stability, and stronger durability in comparison with the traditional electrolytic capacitors.[3] According to the energy-storage mechanism, supercapacitors can be classified into three main types: (i) electrical double-layer capacitors using ion adsorption−desorption at the electrode/electrolyte interface; (ii) pseudocapacitors using redox reactions (oxidation/reduction reaction) at the electrode/electrolyte interface; and (iii) hybrid supercapacitors, which combine the features of electrical double-layer capacitors and pseudocapacitors.[4−7] Pseudocapacitors, also called faradic capacitors, store energy by faradic reactions at the electrode/electrolyte interface.[8] Based on the working mechanism of pseudocapacitors, various types of metal oxides, transition metal oxides, and metal−organic frameworks can be applied as electrode layers, which enhance the energy density. Currently, two-dimensional metal oxides have been studied for pseudocapacitors due to their large specific surface area, fast ionic diffusion, and high electrical conductivity.[9,10] The vanadium oxide family, with several oxidation states, is one of the promising candidates due to its cost-effectiveness, ease of synthesis, high conductivity, and durability.[11,12] Therefore, in this report, two-dimensional $NH_4V_3O_8$ materials with nanoflakes in the meter scale with a high specific surface area have been studied as electrode layers in supercapacitors.

Along with the rapid development of renewable energy sources, the field of energy conversion has attracted much attention, strongly focusing on producing green fuels. Among various types of energy conversion, hydrogen energy from the water-splitting process via electrochemical reaction is considered to be a clean and economical energy with a higher energy density in comparison with chemical fuels.[13−15] Currently, research is strongly focused on hydrogen energy from the water-splitting reaction due to its stability, lack of CO

Received: April 15, 2022
Accepted: June 28, 2022
Published: July 11, 2022

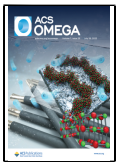





https://doi.org/10.1021/acsomega.2c02375
*ACS Omega* 2022, 7, 25433−25442

emission, and high efficiency.[13] Typically, during the water-splitting reaction in an acidic medium ($H_2O \rightarrow H_2 + 1/2O_2$), two reactions occur under the applied power: $H_2$ evolution reaction at the cathode (HER: $2H^+ + 2e^- \rightarrow H_2$) and $O_2$ evolution reaction at the anode (OER: $4OH^- \leftrightarrow 2H_2O + O_2 + 4e^-$).[16,17] At present, noble-metal materials (Pt, Rh, Ir, etc.) are being used as catalysts to produce $H_2$, which contribute up to 4% of the supply worldwide, but they are expensive, unstable, and less abundant on earth.[18,19] Therefore, the design of low-cost, earth-abundant, and efficient materials for stable electrochemical applications including energy conversion and storage is an issue of urgent concern in the field of renewable energies. Currently, two-dimensional (2D) materials of metals and composites serve as core materials due to (i) their large specific surface area with nanoflake layers, (ii) tunable electronic structure, and (iii) mechanical strength and high durability, which enhance the active sites for improved catalytic performances.[20,21] In addition, two-dimensional metal oxides (2D-MOs) are promising candidates due to their unique properties such as high conductivity, high mechanical strength, catalytic capability, and good electrochemical behavior.[22] In comparison with bulk metal oxide materials, 2D metal oxide materials have a higher specific surface area and good electrochemical behavior due to their better exposed active sites.[23] Moreover, the faradic reaction of 2D MO electrode materials at the electrode/electrolyte interface can enhance the electrochemical performance.[24] Among them, 2D-$NH_4V_3O_8$ nanoflakes are excellent candidates for energy-storage and conversion applications because of their low cost, fast synthesis, higher specific surface area compared with other MO materials, $NH_4$ molecular connections with VO layers to prevent the destruction of the structure, and hydrogen bonding between $NH_4$ and VO, which improves their stability.[25−27] Accordingly, in this work, 2D-$NH_4V_3O_8$ nanoflakes are introduced as cathode materials to study the hydrogen evolution reaction.

In the process of assembling the electrochemical capacitors (or supercapacitors) from 2D MO materials, the advantages of the 2D materials can be preserved well, which enhance the electron-transport kinetics via the uniformity of the electrode/electrolyte interface layer.[28] Moreover, the large surface area of 2D MO electrodes provides an excellent environment of ion pools for fast ion diffusion during the charge−discharge process.

Herein, we develop a cost-effective and simple process to prepare $NH_4V_3O_8$ nanoflakes using a two-step synthesis method: (1) simple hydrothermal reaction and (2) calcination. The final $NH_4V_3O_8$ product shows a good 2D structure that serves as a single material with two simultaneous applications: electrocatalysts for the hydrogen evolution reaction and electrochemical capacitors for supercapacitors. The $NH_4V_3O_8$ nanoflakes are considered as good HER candidates with an exceptional overpotential value of 310 mV at 10 mA $cm^{-2}$ with a good Tafel slope of 90 mV $decade^{-1}$. The supercapacitor electrode slurry made from $NH_4V_3O_8$ nanoflakes displays the highest specific capacitance of 274 F $g^{-1}$ at 0.5 A $g^{-1}$, with an excellent energy density of 38 W h $kg^{-1}$. In summary, the $NH_4V_3O_8$ material shows high durability with the corresponding electrochemical stability to maintain the morphology.

## 2. EXPERIMENTAL SECTION

**2.1. Materials.** Sodium sulfate ($Na_2SO_4$), standard 0.5 M $H_2SO_4$ (1 N) solution as the aqueous electrolyte for the HER study, acid oxalic ($HO_2C-CO_2H$), 1-methyl-2-pyrrolidone (NMP), and dimethylformamide [$HCON(CH_3)_2$, DMF] were obtained from Sigma-Aldrich. Ammonium metavanadate ($NH_4V_3O_8$), ammonium hydroxide ($NH_4OH$), and acetic acid ($CH_3COOH$) were obtained from Alfa Aesar. The carbon paper substrate (A4 size, 0.15 mm thickness) was obtained from HOMYTECH CO., LTD., Taiwan. Ultrapure water was prepared by the Millipore Milli-Q UF system at room temperature with a resistivity of 18.2 MΩ cm.

**2.2. Preparation of 2D $NH_4V_3O_8$ Nanoflakes and Material Characterization.** 2D-$NH_4V_3O_8$ was synthesized by a simple hydrothermal method. Typically, 1 g of $NH_4VO_3$ was dissolved in 20 mL of DI water to obtain a dark-yellow solution. Then, pure acid acetic was added slowly to the $NH_4VO_3$ solution with constant stirring until a pH of 6 to obtain an orange solution. This orange solution was transferred into a 100 mL Teflon-lined hydrothermal stainless steel autoclave and heated at 160 °C for 48 h before cooling down naturally to room temperature (27 °C). Finally, the 2D-$NH_4V_3O_8$ target material was collected, washed with DI water, and dried at 80 °C for 12 h.

Herein, the structure and morphology of the 2D-$NH_4V_3O_8$ nanoflakes were studied using various equipment, including a scanning electron microscope (SEM, SU800, Hitachi), transmission electron microscope (TEM, JEM-2100F, Joel), X-ray diffractometer (XRD, D2 Bruker) with a Cu K$\alpha$ tube, Raman spectrophotometer (Jobin Yvon-Horiba, with 520 nm excitation wavelength of an Ar laser), X-ray photoelectron spectrometer (nano-Auger/ESCA electron spectroscopy vs XPS), and Fourier transform infrared (FTIR) spectrometer (PerkinElmer), and by Brunauer−Emmett−Teller (BET) analysis using Micromeritics ASAP 2020.

**2.3. Electrochemical Characterizations.** The catalyst ink was prepared by adding 3 mg of 2D-$NH_4V_3O_8$ nanoflakes to 1 mL of DMF with constant stirring for 2 days to obtain a homogeneous solution for electrochemical studies of HER. For comparison, a commercial $V_2O_5$ product was also prepared by the same process as above.

Furthermore, the 2D-$NH_4V_3O_8$ slurry for electrochemical supercapacitor studies was prepared by mixing together 8 mg of $NH_4V_3O_8$ (80 wt %), 1 mg of CNT (10 wt %), 1 mg of PVDF (1 wt %), and 0.2 mL of NMP with constant stirring for 2 days to obtain a uniform active slurry. Then, this active slurry was stored for further electrochemical supercapacitor measurements.

To prepare the working electrode for the electrochemical catalyst, 2 $\mu$L of the $NH_4V_3O_8$ active slurry was coated on the GCE (3 mm in diameter; 0.214 mg $cm^{-2}$) and dried at 60 °C for 1 day. Finally, 2 $\mu$L of Nafion (5% in EtOH) was covered on the $NH_4V_3O_8$-modified glassy carbon electrode and dried naturally. Here, a three-electrode system was studied using a carbon rod counter electrode (diameter 0.5 cm, length 20 cm), an Ag/AgCl (3 M NaCl) reference electrode, and a 0.5 M $H_2SO_4$ aqueous electrolyte. Linear sweep voltammetry (LSV) was performed in the range of 0−0.8 V vs RHE at a scan rate of 5 mV $s^{-1}$. The electrochemical impedance study (EIS) data were analyzed from 100 mHz to 100 kHz at an amplitude of 5 mV. The stability test was performed following $i-t$ curves at an overpotential point over a period of 48 h. The HER mechanism in an acidic electrolyte can be illustrated by the following equations[16,17]


https://doi.org/10.1021/acsomega.2c02375
ACS Omega 2022, 7, 25433−25442

**Table 1. Lattice Constants**

| $NH_4V_3O_8$ | $a$ (Å) | $b$ (Å) | $c$ (Å) | $\alpha$ (deg) | $\beta$ (deg) | $\gamma$ (deg) |
|---|---|---|---|---|---|---|
| GGA | 4.92066 | 8.28296 | 7.62480 | 90.000 | 94.8493 | 90.000 |
| GGA + $U$ | 5.09855 | 8.58216 | 7.85297 | 90.000 | 96.4311 | 90.000 |
| HSE06 | 4.87999 | 8.10927 | 7.48049 | 90.000 | 93.4884 | 90.000 |
| experiment[8] | 4.993(7) | 8.423(1) | 7.849(1) | 90.000 | 96.426(3) | 90.000 |
| experiment[9] | 4.975(8) | 8.413(14) | 7.855(6) | 90.000 | 96.39(6) | 90.000 |

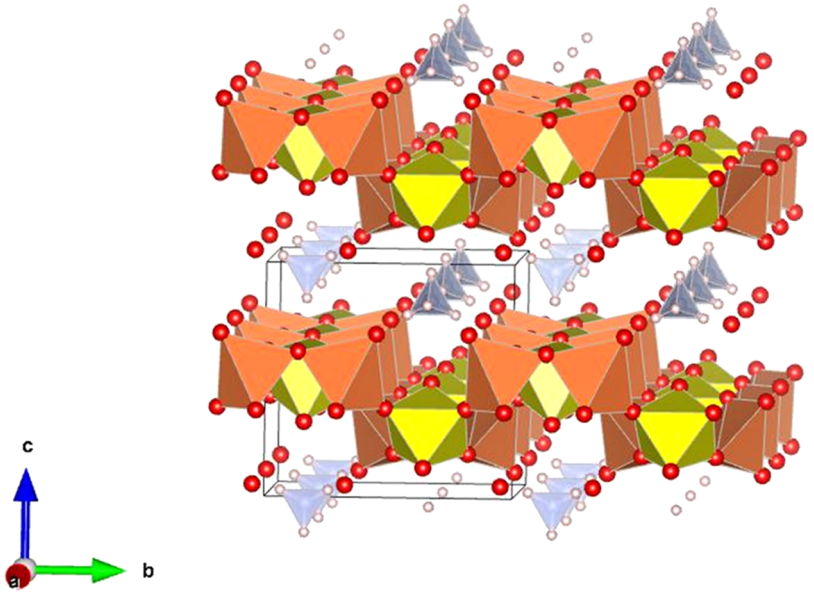


**Figure 1.** Crystal structure of $NH_4V_3O_8$. The twisted zigzag layers of $VO_5$ and $VO_6$ are denoted by yellow and orange colors, respectively, whereas the $NH_4$ groups are in gray and located in the interlayer space.

Volmer reaction of the discharge step:

$$H_3O^+ + e^- \rightarrow H_{ads} + H_2O \quad (1)$$

Tafel reaction of the recombination–desorption step:

$$H_{ads} + H_{ads} \rightleftharpoons H_2 \quad (2)$$

Heyrovsky reaction of the desorption step:

$$H_{ads} + H_3O^- + e^- \rightarrow H_2 + H_2O \quad (3)$$

The Tafel slope can be calculated using the Tafel equation:

$$\eta = b \times \log j + a \quad (4)$$

where $\eta$ is the overpotential, $b$ is the Tafel slope, $j$ is the current density, and a is a constant.

For electrochemical capacitor studies, the working electrodes were prepared by coating 20 $\mu$L of the 2D-$NH_4V_3O_8$ active slurry on a carbon paper substrate (1 × 1 $cm^2$) and drying at 80 °C for 2 days. Here, one Pt plate (1 × 2 $cm^2$) served as the counter electrode and Ag/AgCl as the reference electrode. This three-electrode system was measured in a 1 M $Na_2SO_4$ aqueous electrolyte by CV, EIS, and galvanostatic charge–discharge (GCD) measurements. The specific capacitance was calculated by the following equation:[29,30]

$$C = \frac{I \times \Delta t}{\Delta V \times m_{ac}} \quad (5)$$

From the GCD curves, the energy density ($E$, W h $kg^{-1}$) and power density ($P$, W $kg^{-1}$) could be calculated by the following equations, respectively:[29,30]

$$E = \frac{C \times (\Delta V)^2}{2} \times \frac{1000}{3600} \quad (6)$$

$$P = \frac{E \times 3600}{\Delta t} \quad (7)$$

where $I$ (A) is the discharge current, $\Delta t$ is the discharge time, $\Delta V$ is the potential voltage, and $m_{ac}$ is the weight of the active materials (including the binder).

Moreover, the specific capacitance can be calculated from CV curves by the following equation:[27]

$$C = \frac{\int_{E_i}^{E_f} I(E)\mathrm{d}E}{m \cdot v \cdot (E_f - E_i)} \quad (8)$$

where $E_i$ and $E_f$ are the initial and final voltages, respectively, $v$ is the scan rate (V $s^{-1}$), $m$ is the weight of the active material, and $(E_f - E_i)$ is the width of the potential window.

## 3. RESULTS AND DISCUSSION

**3.1. Computational Results.** *3.1.1. Computational Details.* Density functional theory (DFT) computation was performed using the Vienna ab-initio Simulation Package (VASP) code.[31−35] Electron–ion interactions and electron-exchange correlations were described by the projector augmented wave (PAW) potentials and the general gradient approximation (GGA) applying the Perdew–Burke–Ernzerhof (PBE) functional, respectively.[36,37] For comparison purposes, GGA, GGA + $U$, and HSE06 methods were used to decrease the self-interaction error, which selectively incorporates an



https://doi.org/10.1021/acsomega.2c02375
ACS Omega 2022, 7, 25433−25442

energy correction to localized electron states of d or f orbitals whose self-interaction is quite large. The optimization of all atomic positions and lattice constants used the conjugate gradient scheme to relax the geometrical structure until the components of the forces on each atom were on the order of $10^{-4}$ eV Å$^{-1}$. The energy cutoff was set to 400 eV to correct the accuracy of the simulated data. We used the bulk unit cell of $NH_4V_3O_8$ containing 32 (N/H/V/O ~2/8/6/16) atoms, which corresponded to two units with the $NH_4V_3O_8$formula. A 2 × 2 × 2 *k*-point mesh for a primitive $NH_4V_3O_8$ unit cell was set. Geometrical structures and electronic properties of $NH_4V_3O_8$ are analyzed by means of DFT calculations.

*3.1.2. Crystal Structure.* The optimized lattice constants of $NH_4V_3O_8$ obtained from our DFT calculations (Table 1) are in agreement with the experimental values.[38,39] The lattice parameters calculated using the GGA + *U* functional for $NH_4V_3O_8$ are $a$ = 5.09855 Å, $b$ = 8.58216 Å, $c$ = 7.85297 Å, and $\beta$ = 96.4311°, which were confirmed with respect to the reference values from JCPDS card no. 088-1473.[38] According to the results presented in Table 1, the GGA and GGA + *U* functionals provide a more accurate description of the lattice parameters than the HSE06 functional.

$NH_4V_3O_8$ crystallizes in the monoclinic $P2_1/m$ space group. As illustrated in Figure 1, $NH_4V_3O_8$ has a layered structure including two basic structural units of the $VO_6$ octahedron and $VO_5$ square pyramids, respectively. Here, $NH_4^+$ cations are located on the sites between the vanadium oxide layers. Moreover, each pair of $VO_5$ square pyramids is connected by an edge to form a double $V_2O_8$ group, and the $V_2O_8$ groups are bridged by sharing corners to create a twisted zigzag chain. It is clearly seen that one $VO_6$ octahedron is associated with two $V_2O_8$ sets at two edges and with two alternating $V_2O_8$ sets at two corners. These twisting and turning chains are detained together over the $VO_6$ octahedron by sharing angles and edges in turn to form a layered structure parallel to the (001) plane. Notably, N−H−O hydrogen bonds are present between the vanadium oxide layer and the $NH_4^+$ cations. In the first $V_5^+$ site, $V_5^+$ is bonded in the five-coordinate geometry to five oxygen atoms, and the V−O bond lengths range from 1.63 to 1.93 Å. In the second $V_5^+$ site, $V_5^+$ is bonded in a six-coordinate geometry to six oxygen atoms, and the V−O bond lengths range from 1.65 to 2.35 Å. There are five inequivalent oxygen sites. In the first oxygen site, oxygen is bonded in a single-bond geometry to one $V_5^+$ atom. In the second oxygen site, it is bonded in a two-coordinate geometry to three $V_5^+$ atoms. In the third oxygen site, it is bonded in a distorted trigonal non-coplanar geometry to three $V_5^+$ atoms. In the fourth oxygen site, it is bonded in a single-bond geometry to one $V_5^+$ atom. In the fifth oxygen site, it is bonded in a bent 120-degree geometry to two $V_5^+$ atoms.

*3.1.3. Electronic Structures.* The electronic band structure and the density of states (DOS) of the $NH_4V_3O_8$ crystal are calculated using three functionals, GGA, GGA+*U* (U = 3.5 eV), and HSE06. $NH_4V_3O_8$ is a magnetic semiconductor with a band gap of 2.1 eV.[40,41] The electronic structure of $V_3H_4NO_8$ calculated using the GGA functional exhibits an indirect band gap of 1.942 eV between the Γ point of the valence band and the A point of the conduction band; the direct band gap at the Γ point is considerably larger by ~0.098 eV. Using the GGA + *U* ($U$ = 3.5 eV) functional, the indirect band gap is 2.166 eV and the direct band gap is 2.318 eV. Meanwhile, using the HSE06 functional, the indirect band gap is 3.412 eV and the direct band gap is 3.618 eV. These results showed that the GGA and GGA + *U* functionals provide more accurate bandgap energies of $NH_4V_3O_8$ compared with the HSE06 functional. The calculated band structures and DOS of $V_3H_4NO_8$ are visualized in Figure 2a using the GGA functional

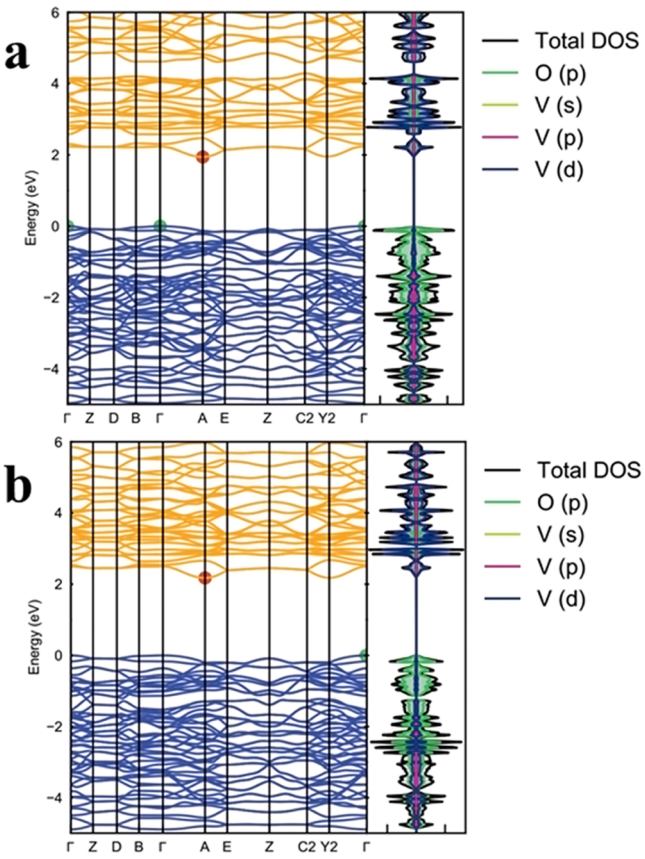


**Figure 2.** Electronic band structure and density of states of $V_3H_4NO_8$ using (a) GGA and (b) GGA + *U* ($U$ = 3.5 eV).

and in Figure 2b using the GGA + *U* ($U$ = 3.5 eV) functional. The lowest conduction band has the foremost V 3d. The highest occupied states are formed by the band of well-localized V 3d states, whereas the wide valence band in the range of −4 eV to the Fermi level is composed predominantly of O 2p states. In general, the DOS apparently resembles the formation of covalent V−O bonds within the anionic $V_3O_8$ structure. The relative position governing V 3d−O 2p overlaps in the valence band marks a certain flexibility of the $V_3O_8$ network for association in redox reactions and a low ability of $NH_4^+$ cations for reduction.

**3.2. $NH_4V_3O_8$ Powder Characterizations.** Figure 3a shows the results of Raman spectroscopy of $NH_4V_3O_8$ with strong clear 2$\theta$ peaks at 240, 372, 427, 673, 813, 963, and 994 cm$^{-1}$, which agree with the literature data and indicate the existence of two states of $VO_5$ and $VO_6$ (Figure 1).[42−44] The two peaks around 963 correspond to V=O stretching modes of the distorted octahedron and the peak at 994 cm$^{-1}$ belongs to distorted pyramids.[43,44] The strong peak at 813 cm$^{-1}$ corresponds to the V−O stretching bond.[44] The series of clear peaks at 514, 556, and 673 cm$^{-1}$ are assigned to V−O−V stretching bonds.[43,44] Other peaks at frequencies below 400 cm$^{-1}$ belong to V−O and N−H bending modes.[45] The phase structure of $NH_4V_3O_8$ samples was studied by X-ray diffraction (XRD), and the results are depicted in Figure 3b with various


https://doi.org/10.1021/acsomega.2c02375
ACS Omega 2022, 7, 25433−25442

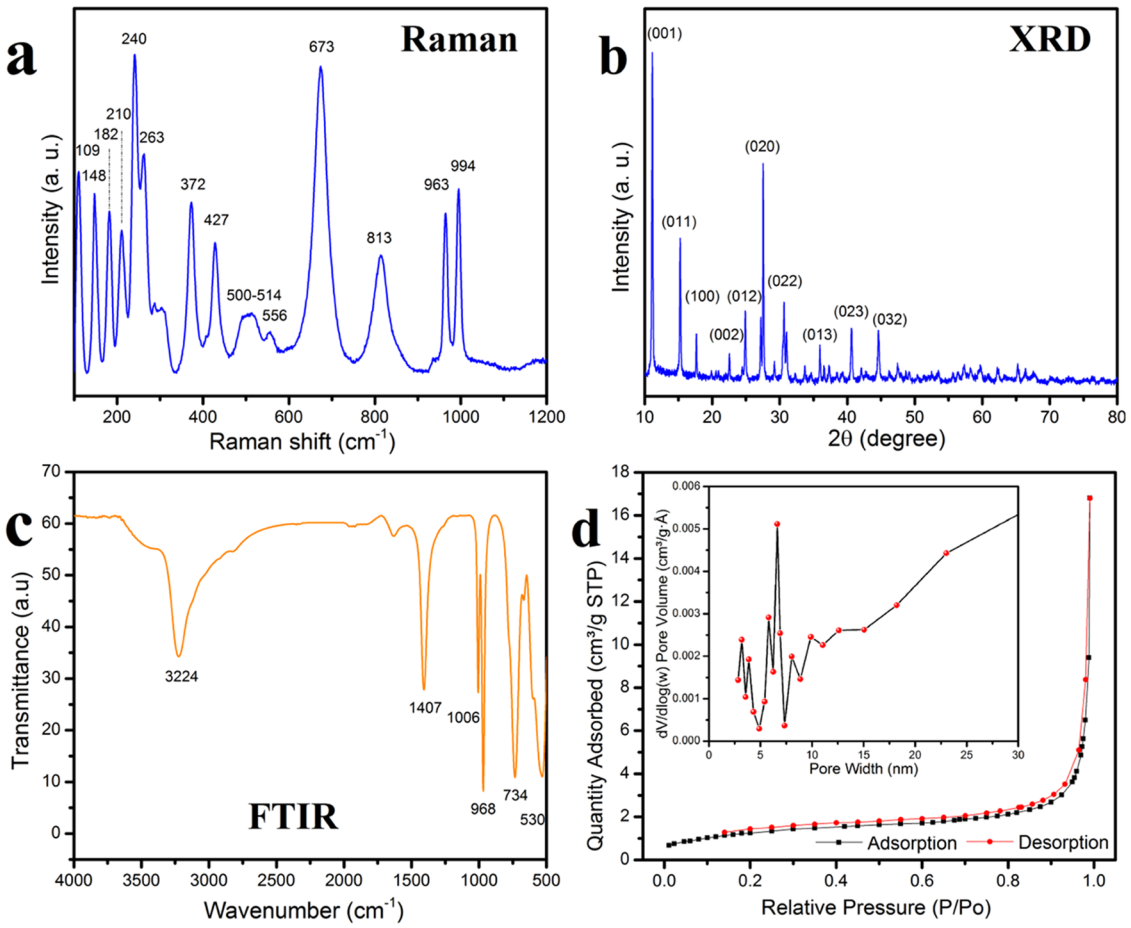


**Figure 3.** (a) XRD pattern, (b) Raman spectra, (c) FTIR spectra, and (d) adsorption/desorption isotherms of $N_2$ with the pore size distribution.

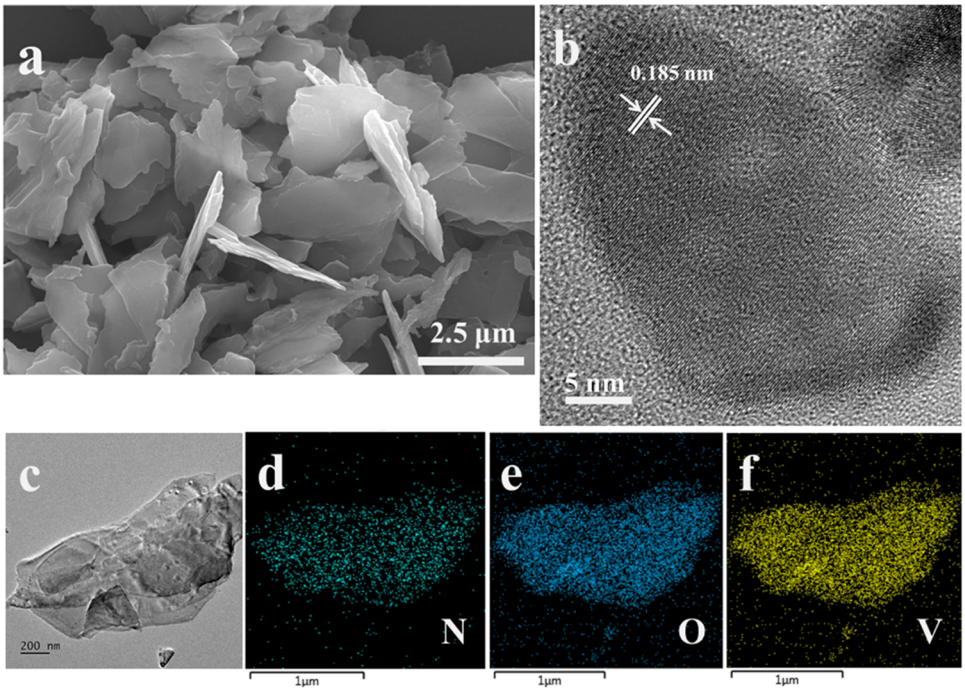


**Figure 4.** (a) SEM, (b) HRTEM, and (c–f) TEM elemental-mapping images of $NH_4V_3O_8$ nanoflakes.

clear peaks corresponding to the (001), (011), (100), (002), (012), (020), (022), (013), (023), and (032) planes. These diffraction peaks reveal the monoclinic form of $NH_4V_3O_8$ according to JCPDS card no. 088-1473, which is in good agreement with the simulated results and previous literature.[44,46,47] No impurities were detected, indicating the



https://doi.org/10.1021/acsomega.2c02375
ACS Omega 2022, 7, 25433−25442

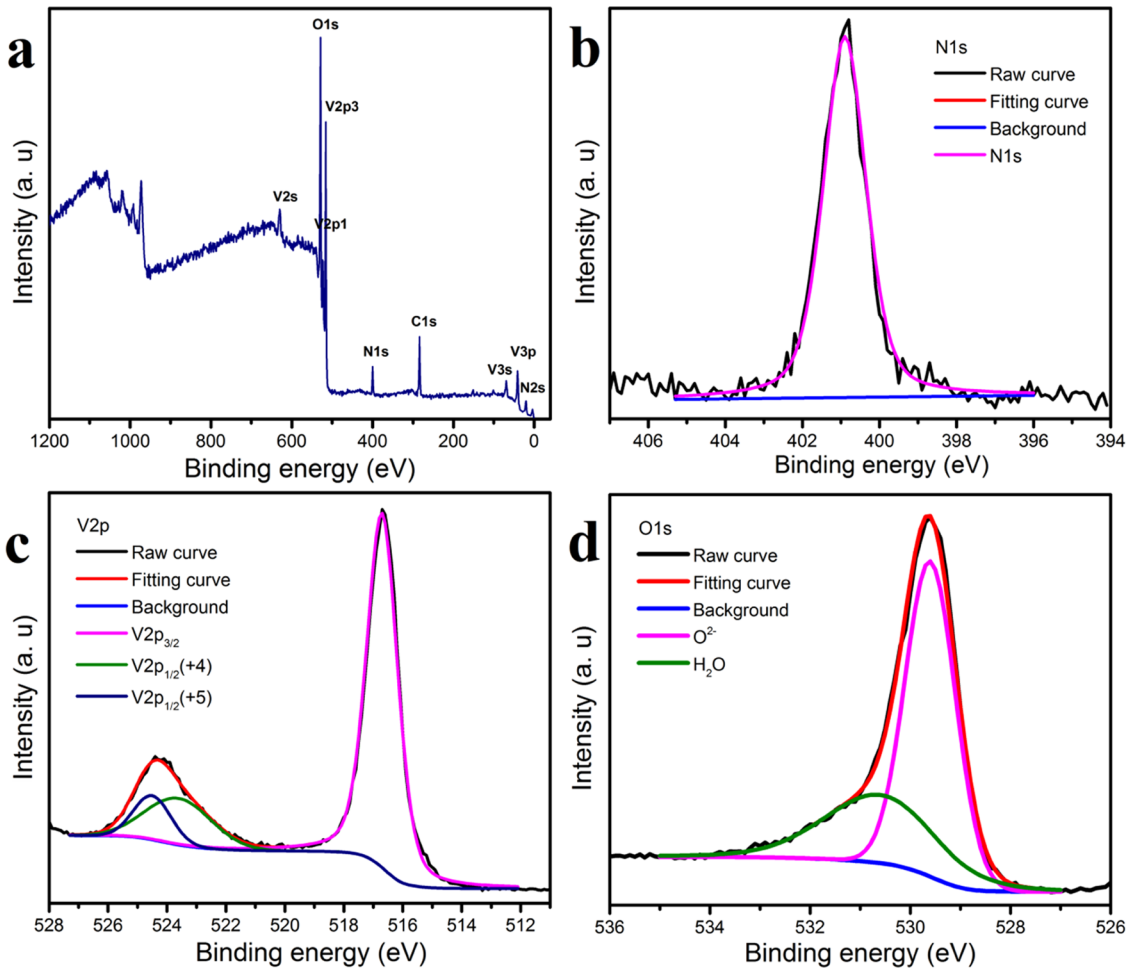


**Figure 5.** XPS spectra of $NH_4V_3O_8$ nanoflakes: (a) survey spectra, (b) N 1s, (c) V 2p, and (d) O 1s.

appropriate method of synthesis and highly crystalline form of the $NH_4V_3O_8$ sample. The functional groups of $NH_4V_3O_8$ were identified by FTIR analysis and are illustrated in Figure 3c. There are various strong peaks at 3224, 1407, 1006, 968, 734, and 530 $cm^{-1}$, which correspond to the different excitations of the $NH_4V_3O_8$ sample.[44] The absorption peak at 530 $cm^{-1}$ belongs to the stretching vibration of oxygen coordinates with vanadium atoms in $VO_5$ square pyramids and the $VO_6$ octahedron. The band at 734 $cm^{-1}$ belongs to a symmetrical stretching vibration of the V−O−V bond.[48,49] The bands at 968 and 1006 $cm^{-1}$ are assigned to the stretching vibration of V═O.[48,49] The band at 1407 $cm^{-1}$ is attributed to $NH_4^+$ groups.[44,48,49] The clear strong peak at 3224 $cm^{-1}$ shows the existence of hydrogen bonds.[44] The specific surface area and porosity were determined from the nitrogen adsorption−desorption isotherm analysis of $NH_4V_3O_8$ and is depicted in Figure 3d. The $NH_4V_3O_8$ powder exhibits a good value of 4.7 $m^2$ $g^{-1}$, which agrees with the values of 2D metal oxide materials. The increasing nitrogen adsorption at a high relative pressure illustrates the appearance of macropores in the sample, whereas the narrow open hysteresis loop from 0.9 to 0.2 of $P/P_0$ shows the presence of mesopores.[50] As presented in the inset in Figure 3d, the pore size distribution shows an adsorption average pore width ($4V/A$ by BET) of ∼22 nm. The BJH adsorption and BJH desorption average pore width ($4V/A$) are 29.1 and 25.3 nm, respectively.

Figure 4 shows the surface morphology of the $NH_4V_3O_8$ sample by SEM and TEM measurements. It can be seen that $NH_4V_3O_8$ exhibits a 2D structure of thin nanoflakes, which are composed of many sheet layers. Figures 4a and S1a clearly illustrate the lamellar structures with a random arrangement, which can form porous electrodes with a high active surface and high specific surface area. Moreover, the high-resolution HR-TEM images of the $NH_4V_3O_8$ sample in Figures 4b and S1b show the perfect interlayer distance with a lattice spacing of 0.185 nm, which belongs to the $NH_4V_3O_8$ nanoflakes and match well with the XRD and Raman results. Here, $NH_4V_3O_8$ nanoflakes were very thin and displayed a large size and high uniformity, with a width of up to 2 $\mu$m.

Further, the successful $NH_4V_3O_8$ structure is proven by TEM mapping, where N, O, and V elements are homogeneously overlapping throughout the entire sample. Note that the exemplary results obtained from the selected area TEM measurement in Figures 4c−f and S1c−f confirm precisely the elements of $NH_4V_3O_8$ nanoflakes. In this study, to understand the growth mechanism of 2D $NH_4V_3O_8$ nanoflakes, the basic reaction for the preparation of $NH_4V_3O_8$ nanoflakes can be described by the following formula:[39,43]

$$3NH_4VO_3 + 2CH_3COOH \rightarrow NH_4V_3O_8 + 2NH_4OCOCH_3 + H_2O$$



https://doi.org/10.1021/acsomega.2c02375
ACS Omega 2022, 7, 25433−25442

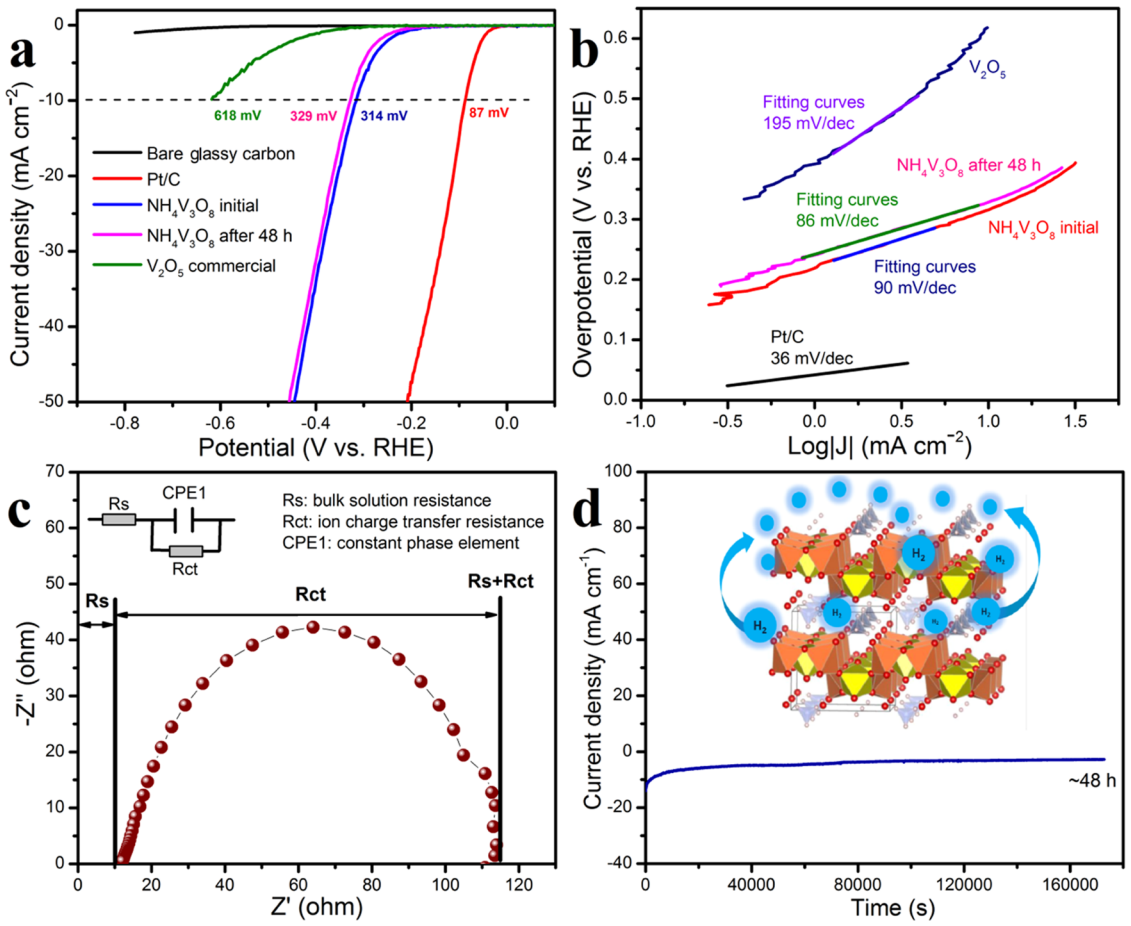


**Figure 6.** Electrolytic properties of $NH_4V_3O_8$: (a) LSV plots, (b) Tafel plots, (c) EIS plots, and (d) stability at 10 mA cm$^{-2}$ over a period of 48 h.

Figure 5 shows the chemical composition and valence state of pure $NH_4V_3O_8$ by the XPS analysis. Figure 5a illustrates the XPS survey spectra, which reveal the expected ratio of C, V, O, and N elements. The XPS peak of N 1s in Figure 5b shows only one centered peak at 401 eV. The V 2p peak shown in Figure 5c can be divided into three main peaks at around 516.7, 523.5, and 524.5 eV, which correspond to V $2p_{3/2}$, V $2p_{1/2}$ (+4), and V $2p_{1/2}$ (+5), respectively.[51,52] The O 1s spectrum in Figure 5d illustrates the existence of $O^{2-}$ at 529.6 eV and $H_2O$ at 530.6 eV.[51] In summary, it can be confirmed that $NH_4V_3O_8$ with high purity can be successfully applied as the working electrode for further studies on energy storage and conversion.

**3.3. Hydrogen Evolution Reaction Electrocatalytic Activity of $NH_4V_3O_8$.** The electrocatalytic properties of $NH_4V_3O_8$ were measured in standard 0.5 M $H_2SO_4$ with a three-electrode system, and the results are shown in Figure 6. Moreover, commercial $V_2O_5$ was also prepared for comparison in this study. As shown in Figure 6a, the polarization (linear sweep) curves of $NH_4V_3O_8$ at the initial time and after 48 h show excellent durability, with HER onset overpotential $\eta$ values of 314 and 329 mV at a current density of −10 mA cm$^{-1}$, respectively. Accordingly, the HER performance of $NH_4V_3O_8$ was investigated and compared with commercial $V_2O_5$ and Pt. The $V_2O_5$ displayed a value of 618 mV, whereas the commercial Pt/C has a low overpotential value of 87 mV at the same current density of −10 mA cm$^{-1}$. These better results of $NH_4V_3O_8$ nanoflakes in comparison with those of commercial $V_2O_5$ may be due to the good electron transfer during the electrocatalytic process, which provides more electrons for $H^+$ reduction to $H_2$ on the exposed edges of the $NH_4V_3O_8$ nanoflakes. Another reason is the porous structure arising from the random arrangement of $NH_4V_3O_8$ nanoflake layers, which provide highly exposed active sites. To investigate the HER of $NH_4V_3O_8$ nanoflakes in detail, Tafel slopes were calculated following eq 4, and the results are shown in Figure 6b. Here, the Tafel slopes of $NH_4V_3O_8$ from the LSV curves indicate that the charge-transfer kinetics at the initial time and after 48 h are 90 and 86 mV dec$^{-1}$, which are much lower than those of commercial $V_2O_5$ (195 mV dec$^{-1}$). These results are higher than those of Pt (86 mV dec$^{-1}$) but provide promising data for further development of 2D $NH_4V_3O_8$ materials. The stable Tafel slope of $NH_4V_3O_8$ after 48 h of electrochemical measurement shows that this material is ideal for the HER study. Moreover, the electrode kinetics of the $NH_4V_3O_8$ nanoflake material was also investigated using EIS measurements, as shown in Figure 6c. The equivalent series resistance ($R_S$) and charge-transfer resistance ($R_{CT}$) were 12 and 112 Ω (Figure S3 and Table S1), respectively, indicating the high electrical conductivity, highly conductive electrode−electrolyte interface, and good internal resistance of $NH_4V_3O_8$ nanoflakes, which make them an excellent HER catalyst.[53] The $i$−$t$ curves of $NH_4V_3O_8$-modified glassy carbon electrodes at −10 mA cm$^{-2}$ after 48 h of chronoamperometry measurement shown in Figure 6d suggest the good stability of $NH_4V_3O_8$ for HER. Although the $NH_4V_3O_8$-modified glassy carbon electrode shows a decrease in the slope of LSV plots and also the current density after a



https://doi.org/10.1021/acsomega.2c02375
ACS Omega 2022, 7, 25433−25442

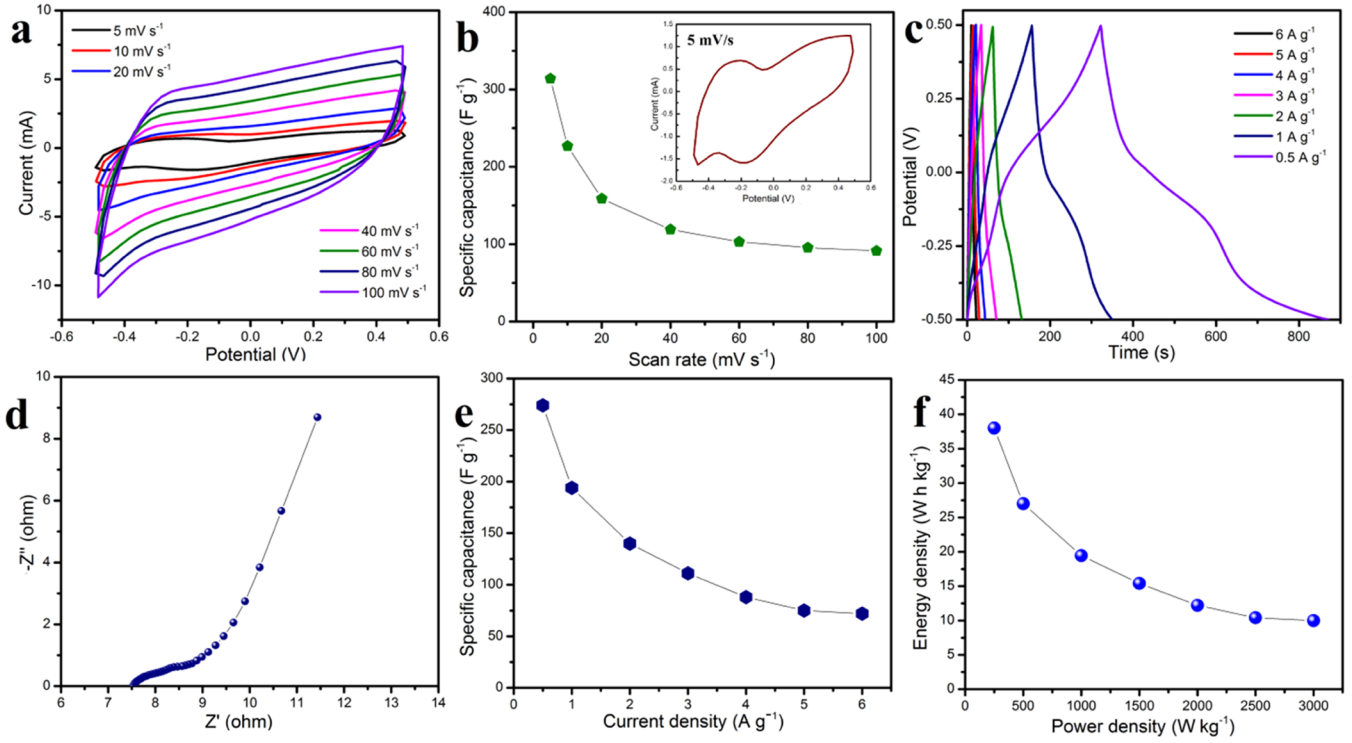


**Figure 7.** Electrochemical properties of the three-electrode system for supercapacitor measurements: (a) CV curves, (b) specific capacitances at various scan rates, (c) GCD curves, (d) EIS plot, (e) specific capacitance at various current densities, and (f) energy density as a function of power densities.

long-term test of 48 h due to decomposition at the electrode surface, it is still within the acceptable range for HER application. Moreover, the SEM images in Figure S2 of the $NH_4V_3O_8$ material after electrochemical studies of HER demonstrate the stable 2D nanoflakes, which indicate the good structure after long electrochemical measurements.

**3.4. Electrochemical Supercapacitor Studies.** Based on the high specific surface area of transition metal oxide materials, 2D structures with highly exposed sites for HER, and good conductivity, $NH_4V_3O_8$ is expected to be outstanding for electrochemical capacitor applications. The electrochemical characteristics and performance of the three-electrode system are presented in Figure 7. The cyclic voltammetry (CV) of the $NH_4V_3O_8$ working electrode in the three-electrode system in a 1 M $Na_2SO_4$ aqueous electrolyte is shown in Figure 7a. It can be seen that the CV curves have strong redox and reduction peaks at low scan rates of 5 mV $s^{-1}$, which indicate the redox reaction during scan progress. This could be attributed to the electrochemical capacitance behavior of the working electrode. From Figure 7b, a high specific capacitance of 314 F $g^{-1}$ was obtained at a scan rate of 5 mV $s^{-1}$. Despite the high scan rate of 100 mV $s^{-1}$, an acceptable specific capacitance of 91.4 F $g^{-1}$ is still obtained. The galvanostatic charge−discharge (GCD) curves at various current densities are shown in Figure 7c. At all current densities, the GCD curves display a nonsymmetrical triangular shape due to the redox reaction during the charge−discharge process. Here, the redox reaction is very strong at the electrode/electrolyte interface, which is attributed to the capacitance behavior. For further investigation of the contribution of the redox reaction, the Coulombic efficiency was investigated, following the Coulombic efficiency equation:[29]

$$\varepsilon = (t_{discharge}/t_{charge}) \times 100\% \quad (9)$$

The $\varepsilon$ values at various different current densities of 6, 5, 4, 3, 2, 1, and 0.5 A $g^{-1}$ are 120, 107, 104, 108, 113, 124, and 170%, respectively.

To understand the electrical conductivity and resistance of the working electrode and aqueous electrolyte, electrochemical impedance spectroscopy (EIS) was carried out, and the results are presented in Figure 7d via the Nyquist plot. Here, a high-frequency intercept shows the solution resistance, with a nearly semicircular curve corresponding to the charge-transfer resistance.[54] The equivalent series resistance in this case shows a low value of 7.5 Ω, which indicates the good electrical conductivity of the working electrode and excellent ion diffusion. The equivalent series resistance is the sum of the working electrode resistance, the resistance of the electrolyte, the resistance of the electrode/electrolyte interface, and the internal resistance of the electrode material.[29,30] Further, the specific capacitance of the working electrode can be calculated from the GCD curves and is illustrated in Figure 7e. The specific capacitance at a high current density of 6 A $g^{-1}$ is 72 F $g^{-1}$. The maximum specific capacitance is 274 F $g^{-1}$ at 0.5 A $g^{-1}$. Further, the Ragone plot of the $NH_4V_3O_8$ working electrode was calculated from the GCD curves and is illustrated in Figure 7f. At the highest power density of 3000 W $kg^{-1}$, a good energy density of 10 W h $kg^{-1}$ and a high maximum energy density of 38 W h $kg^{-1}$ at a power density of 250 W $kg^{-1}$ were obtained.

In this report, the $NH_4V_3O_8$ nanoflakes showed excellent electrochemical properties, which served well in electrochemical capacitors and HER: (i) the uniformity and high purity of 2D $NH_4V_3O_8$ nanoflakes yield high electrical conductivity, which serves well as the working electrode


https://doi.org/10.1021/acsomega.2c02375
ACS Omega 2022, 7, 25433−25442

layer, allowing fast electron transport; (ii) 2D $NH_4V_3O_8$ nanoflakes are vertically aligned on the surface, which enhances the active sites, which in turn enhance the HER performance; and (iii) the combination between the double layer and the pseudocapacitor of 2D $NH_4V_3O_8$ nanoflakes during the electrochemical process improves the capacitor performance.

## 4. CONCLUSIONS

In conclusion, 2D-$NH_4V_3O_8$ nanoflakes were successfully prepared by a simple and cost-effective method, which provided a high surface area of the 2D structure, good conductivity, and high purity. As a result, the $NH_4V_3O_8$ nanoflakes displayed an outstanding catalytic performance via HER with a low overpotential of 314 mV vs RHE at 10 mA $cm^{-2}$ and a good Tafel slope of 90 mV $dec^{-1}$. Moreover, $NH_4V_3O_8$ also displayed excellent stability after 48 h. Furthermore, 2D $NH_4V_3O_8$ showed a high electrochemical capacitor performance of the three-electrode system of 274 F $g^{-1}$ at 0.5 A $g^{-1}$ and the highest energy density of 38 W h $kg^{-1}$ at a power density of 250 W $kg^{-1}$. This work provides a promising 2D material with two simultaneous applications as an electrocatalyst for HER as well as an electrochemical capacitor for supercapacitors.

## ■ ASSOCIATED CONTENT

### Supporting Information

The Supporting Information is available free of charge at https://pubs.acs.org/doi/10.1021/acsomega.2c02375.

Experimental details regarding SEM, TEM, and fitting of the EIS including the table of elemental composition of 2D-$NH_4V_3O_8$ nanoflakes (PDF)

## ■ AUTHOR INFORMATION


### Corresponding Authors

**Phuoc-Anh Le** − *Institute of Sustainability Science, VNU Vietnam Japan University, Vietnam National University, Hanoi 100000, Vietnam; Faculty of Textile Science and Technology, Shinshu University, Ueda, Nagano 386-0018, Japan*; Email: lephuocanh86@vnu.edu.vn

**Thi Viet Bac Phung** − *Institute of Sustainability Science, VNU Vietnam Japan University, Vietnam National University, Hanoi 100000, Vietnam*; orcid.org/0000-0001-7717-2538; Email: ptv.bac@vju.ac.vn

### Authors

**Van-Qui Le** − *Department of Materials Science and Engineering, National Yang Ming Chiao Tung University, Hsinchu 300093, Taiwan*

**Thien Lan Tran** − *Institute of Sustainability Science, VNU Vietnam Japan University, Vietnam National University, Hanoi 100000, Vietnam; Department of Physics, Hue University of Education, Hue University, Hue 530000, Vietnam*

**Nghia Trong Nguyen** − *School of Chemical Engineering, Hanoi University of Science and Technology, Hanoi 100000, Vietnam*

**Van An Dinh** − *Department of Precision Engineering, Graduate School of Engineering, Osaka University, Suita, Osaka 565-0871, Japan*; orcid.org/0000-0002-7290-7969

Complete contact information is available at: https://pubs.acs.org/10.1021/acsomega.2c02375


### Author Contributions

This manuscript was written through the contributions of all authors. All authors have given approval to the final version of the manuscript.

### Notes

The authors declare no competing financial interest.

## ■ ACKNOWLEDGMENTS

The authors acknowledge the facility support from the JICA Technical Cooperation 2 (TC2) project in VNU Vietnam Japan University under Research Project VJU.JICA.21.01. This research was funded by Vietnam National University, Hanoi (VNU), under Project No. QG.20.62.

## ■ REFERENCES


(1) Yu, Z.; Tetard, L.; Zhai, L.; Thomas, J. Supercapacitor electrode materials: nanostructures from 0 to 3 dimensions. *Energy Environ. Sci.* **2015**, *8*, 702−730.

(2) Zheng, Y.; Jiao, Y.; Jaroniec, M.; Qiao, S. Z. Advancing the Electrochemistry of the Hydrogen Evolution Reaction through Combining Experiment and Theory. *Angew. Chem., Int. Ed.* **2015**, *54*, 52−65.

(3) Li, J.; Qiao, J.; Lian, K. Hydroxide ion conducting polymer electrolytes and their applications in solid supercapacitors: A review. *Energy Storage Mater.* **2020**, *24*, 6−21.

(4) Dong, Y.; Zhu, J.; Li, Q.; Zhang, S.; Song, H.; Jia, D. Carbon materials for high mass-loading supercapacitors: filling the gap between new materials and practical applications. *J. Mater. Chem. A* **2020**, *8*, 21930−21946.

(5) Quispe-Garrido, V.; Calle, G. A. C.; Aguilar, A. B.; Montoya, J. G. R.; López, E. O.; Moncada, A. M. B. Advances in the design and application of transition metal oxide - based supercapacitors. *Open Chem.* **2021**, *19*, 709−725.

(6) Bokhari, S. W.; Siddique, A. H.; Sherrell, P. C.; Yue, X.; Karumbaiah, K. M.; Wei, S.; Ellis, A. V.; Gao, W. Advances in graphene-based supercapacitor electrodes. *Energy Rep.* **2020**, *6*, 2768−2784.

(7) Veerakumar, P.; Sangili, A.; Manavalan, S.; Thanasekaran, P.; Lin, K. C. Research Progress on Porous Carbon Supported Metal/Metal Oxide Nanomaterials for Supercapacitor Electrode Applications. *Ind. Eng. Chem. Res.* **2020**, *59*, 6347−6374.

(8) Balasubramaniam, S.; Mohanty, A.; Balasingam, S. K.; Kim, A. J.; Ramadoss, A. Comprehensive Insight into the Mechanism, Material Selection and Performance Evaluation of Supercapatteries. *Nano−Micro Lett.* **2020**, *12*, 85.

(9) Fleischmann, S.; Mitchell, J. B.; Wang, R.; Zhan, C.; Jiang, D.; Presser, V.; Augustyn, V. Pseudocapacitance: From Fundamental Understanding to High Power Energy Storage Materials. *Chem. Rev.* **2020**, *120*, 6738−6782.

(10) Yu, X.; Yun, S.; Yeon, J. S.; Bhattacharya, P.; Wang, L.; Lee, S. W.; Hu, X.; Park, H. S. Emergent Pseudocapacitance of 2D Nanomaterials. *Adv. Energy Mater.* **2018**, *8*, No. 1702930.

(11) Song, H.; Liu, F.; Luo, M. Insights into the stable and fast lithium storage performance of oxygen-deficient $LiV_3O_8$ nanosheets. *Nano Res.* **2021**, *14*, 814−822.

(12) Song, H.; Li, J.; Luo, M.; Zhao, Q.; Liu, F. Ultra-Thin Mesoporous $LiV_3O_8$Nanosheet with Exceptionally Large Specific Area for Fast and Reversible Li Storage in Lithium-Ion Battery Cathode. *J. Electrochem. Soc.* **2021**, *168*, No. 050515.

(13) Le, P. A.; Le, V. Q.; Tran, T. L.; Nghia, T. N.; Phung, T. V. B. Computation and Investigation of Two-Dimensional $WO_3{\cdot}H_2O$ Nanoflowers for Electrochemical Studies of Energy Conversion and Storage Applications. *ACS Omega* **2022**, *7*, 10115−10126.

(14) Zhao, G.; Rui, K.; Dou, S. X.; Sun, W. Heterostructures for Electrochemical Hydrogen Evolution Reaction: A Review. *Adv. Funct. Mater.* **2018**, *28*, No. 1803291.

(15) Greeley, J.; Jaramillo, T. F.; Bonde, J.; Chorkendorff, I.; Nørskov, J. K. Computational high-throughput screening of electrocatalytic materials for hydrogen evolution. *Nat. Mater.* **2006**, *5*, 909−913.
(16) Yan, Z.; Liu, H.; Hao, Z.; Yu, M.; Chen, X.; Chen, J. Electrodeposition of (hydro)oxides for an oxygen evolution electrode. *Chem. Sci.* **2020**, *11*, 10614−10625.
(17) Sarkar, S.; Peter, S. C. An overview on Pd-based electrocatalysts for the hydrogen evolution reaction. *Inorg. Chem. Front.* **2018**, *5*, 2060−2080.
(18) Gray, H. B. Powering the planet with solar fuel. *Nat. Chem.* **2009**, *1*, 112.
(19) McCrory, C. C. L.; Jung, S.; Ferrer, I. M.; Chatman, S. M.; Peters, J. C.; Jaramillo, T. F. Benchmarking Hydrogen Evolving Reaction and Oxygen Evolving Reaction Electrocatalysts for Solar Water Splitting Devices. *J. Am. Chem. Soc.* **2015**, *137*, 4347−4357.
(20) Kumar, K. S.; Choudhary, N.; Jung, Y.; Thomas, J. Recent Advances in Two-Dimensional Nanomaterials for Supercapacitor Electrode Applications. *ACS Energy Lett.* **2018**, *3*, 482−495.
(21) Yu, Q.; Luo, Y.; Mahmood, A.; Liu, B.; Cheng, H. M. Engineering Two-Dimensional Materials and Their Heterostructures as High Performance Electrocatalysts. *Electrochem. Energy Rev.* **2019**, *2*, 373−394.
(22) Ren, B.; Wang, Y.; Ou, J. Z. Engineering two-dimensional metal oxides via surface functionalization for biological applications. *J. Mater. Chem. B* **2020**, *8*, 1108−1127.
(23) Xia, H.; Xu, Q.; Zhang, J. Recent Progress on Two-Dimensional Nanoflake Ensembles for Energy Storage Applications. *Nano−Micro Lett.* **2018**, *10*, 66.
(24) Qin, J.; Das, P.; Zheng, S.; Wu, Z. S. A perspective on two-dimensional materials for planar micro-supercapacitors. *APL Mater.* **2019**, *7*, No. 090902.
(25) Jiang, H.; Zhang, Y.; Pan, Z.; Xu, L.; Zheng, J.; Gao, Z.; Hu, T.; Meng, C.; Wang, J. $NH_4V_3O_8{\cdot}0.5H_2O$ nanobelts with intercalated water molecules as a high performance zinc ion battery cathode. *Mater. Chem. Front.* **2020**, *4*, 1434−1443.
(26) Kou, L.; Cao, L.; Huang, J.; Yang, J. Facile synthesis of reduced graphene oxide/$NH_4V_3O_8$ with high capacity as a cathode material for lithium ion batteries. *Micro Nano Lett.* **2017**, *12*, 940−943.
(27) Leonardi, S. G.; Primerano, P.; Donato, N.; Neri, G. Behavior of sheet-like crystalline ammonium trivanadate hemihydrate ($NH_4V_3O_8.0.5H_2O$) as a novel ammonia sensing material. *J. Solid State Chem.* **2013**, *202*, 105−110.
(28) Xia, H.; Xu, Q.; Zhang, J. Recent Progress on Two-Dimensional Nanoflake Ensembles for Energy Storage Applications. *Nano−Micro Lett.* **2018**, *10*, 66.
(29) Le, P. A.; Nguyen, V. T.; Yen, P. J.; Tseng, T. Y.; Wei, K. H. A new redox phloroglucinol additive incorporated gel polymer electrolyte for flexible symmetrical solid-state supercapacitors. *Sustainable Energy Fuels* **2019**, *3*, 1536−1544.
(30) Le, P. A.; Le, V. Q.; Nguyen, N. T.; Phung, T. V. B. Food seasoning-derived gel polymer electrolyte and pulse-plasma exfoliated graphene nanosheet electrodes for symmetrical solid-state supercapacitors. *RSC Adv.* **2022**, *12*, 1515−1526.
(31) Hohenberg, P.; Kohn, W. Inhomogeneous Electron Gas. *Phys. Rev.* **1964**, *136*, B864−B871.
(32) Kohn, W.; Sham, L. J. Self-Consistent Equations Including Exchange and Correlation Effects. *Phys. Rev.* **1965**, *140*, A1133−A1138.
(33) Kresse, G.; Hafner, J. Ab initio molecular dynamics for liquid metals. *Phys. Rev. B* **1993**, *47*, 558−561.
(34) Kresse, G.; Joubert, D. From ultrasoft pseudopotentials to the projector augmented-wave method. *Phys. Rev. B* **1999**, *59*, 1758−1775.
(35) Kresse, G.; Furthmüller, J. Efficiency of ab-initio total energy calculations for metals and semiconductors using a plane-wave basis set. *Comput. Mater. Sci.* **1996**, *6*, 15−50.
(36) Perdew, J. P.; Wang, Y. Accurate and simple analytic representation of the electron-gas correlation energy. *Phys. Rev. B* **1992**, *45*, 13244.
(37) Perdew, J. P.; Burke, K.; Ernzerhof, M. Generalized Gradient Approximation Made Simple. *Phys. Rev. Lett.* **1996**, *77*, 3865.
(38) Huang, S. D.; Shan, Y. $NH_4V_3O_8$: A novel sinusoidal layered compound formed by the cation templating effect. *Chem. Commun.* **1998**, *10*, 1069−1070.
(39) Ottmann, A.; Zakharova, G. S.; Ehrstein, B.; Klingeler, R. Electrochemical performance of single crystal belt-like $NH_4V_3O_8$ as cathode material for lithium-ion batteries. *Electrochim. Acta* **2015**, *174*, 682−687.
(40) Bradlyn, B.; Elcoro, L.; Cano, J.; Vergniory, M. G.; Wang, Z.; Felser, C.; Aroyo, M. I.; Bernevig, B. A. Topological quantum chemistry. *Nature* **2017**, *547*, 298−305.
(41) Vergniory, M. G.; Elcoro, L.; Felser, C.; Regnault, N.; Bernevig, B. A.; Wang, Z. A complete catalogue of high-quality topological materials. *Nature* **2019**, *566*, 480−485.
(42) Li, Z.; Zhu, Q.; Huang, S.; Jiang, S.; Lu, S.; Chen, W.; Zakharova, G. S. Interpenetrating network of $V_2O_5$ nanosheets/carbon nanotubes nanocomposite for fast lithium storage. *RSC Adv.* **2014**, *4*, 46624−46630.
(43) Vernardou, D.; Apostolopoulou, M.; Louloudakis, D.; Katsarakis, N.; Koudoumas, E. Hydrothermal growth and characterization of shape-controlled $NH_4V_3O_8$. *New J. Chem.* **2014**, *38*, 2098−2104.
(44) Zakharova, G. S.; Täschner, Ch.; Kolb, T.; Jähne, C.; Leonhardt, A.; Büchner, B.; Klingeler, R. Morphology controlled $NH_4V_3O_8$ microcrystals by hydrothermal synthesis. *Dalton Trans.* **2013**, *42*, 4897−4902.
(45) Twu, J.; Shih, C. F.; Guo, T. H.; Chen, K. H. Raman spectroscopic studies of the thermal decomposition mechanism of ammonium metavanadate. *J. Mater. Chem.* **1997**, *7*, 2273.
(46) Kou, L.; Cao, L.; Huang, J.; Song, J.; Feng, L.; Wang, Y.; Chen, S.; Kajiyoshi, K. Polyethylene glycol (PEG)-assisted synthesis of self-assembled cactus-like $NH_4V_3O_8$ for lithium ion battery cathode. *Scr. Mater.* **2020**, *183*, 75−80.
(47) Lai, J.; Zhou, S.; Cheng, F.; Guo, D.; Liu, X.; Xu, Q.; Yin, D. Efficient and Selective Oxidation of 5-Hydroxymethylfurfural into 2, 5-Diformylfuran Catalyzed by Magnetic Vanadium-Based Catalysts with Air as Oxidant. *Catal. Lett.* **2020**, *150*, 1301−1308.
(48) Zakharova, G. S.; Ottmann, A.; Ehrstein, B.; Klingeler, R. Microwave-assisted hydrothermal synthesis of $NH_4V_3O_8$ microcrystals with controllable morphology. *Mater. Res. Bull.* **2016**, *83*, 225−229.
(49) Kou, L.; Song, J.; Ai, T.; Li, W.; Bao, W.; Deng, Z. Intersperse Super P nanoparticles between $NH_4V_3O_8$ microsheets to increase $Li^+$ diffusion coefficient for lithium-ion battery. *Ionics* **2021**, *27*, 1543−1550.
(50) Nguyen, T. N.; Le, P. A.; Phung, V. B. T. Facile green synthesis of carbon quantum dots and biomass-derived activated carbon from banana peels: synthesis and investigation. *Biomass Convers. Biorefin.* **2022**, *12*, 2407−2416.
(51) Jiang, H.; Zhang, Y.; Pan, Z.; Xu, L.; Zheng, J.; Gao, Z.; Hu, T.; Meng, C.; Wang, J. $NH_4V_3O_8{\cdot}0.5H_2O$ nanobelts with intercalated water molecules as a high performance zinc ion battery cathode. *Mater. Chem. Front.* **2020**, *4*, 1434−1443.
(52) Xu, G.; He, H.; Wan, H.; Liu, R.; Zeng, X.; Sun, D.; Huang, X.; Wang, H. Facile synthesis and lithium storage performance of $(NH_4)_2V_3O_8$ nanoflakes. *J. Appl. Electrochem.* **2016**, *46*, 879−885.
(53) Le, P. A.; Nguyen, V. T.; Le, V. Q.; Lu, Y. C.; Huang, S. Y.; Sahoo, S. K.; Chu, Y. H.; Wei, K. H. One-Step Surface-Plasma-Induced Exfoliation of the Graphite/$WS_2$ Bilayer into Homogeneous Two-Dimensional Graphene/$WS_2$ Nanosheet Composites as Catalysts for the Hydrogen Evolution Reaction. *ACS Appl. Energy Mater.* **2021**, *4*, 5143−5154.
(54) Vardhan, P. V.; Idris, M. B.; Ramanathan, V.; Devaraj, S. Electrodeposited $MnCO_3$ as a High Performance Electrode Material for Supercapacitor. *ChemistrySelect* **2018**, *3*, 6775−6778.


https://doi.org/10.1021/acsomega.2c02375
*ACS Omega* 2022, 7, 25433−25442